PAPER

Check for updates

Solid-state synthesis of Si₁₋ₓGeₓ nanoalloys with composition-tunable energy gaps and visible to near infrared optical properties†

Griffin C. Spence,[a] David S. Pate, [ID][b] Corentin Villot,[a] Roshana M. Fouzie,[a] Lisa S. Graves,[a] Ka Un Lao, [ID][a] Ümit Özgür[b] and Indika U. Arachchige [ID] *[a]

Si₁₋ₓGeₓ alloy nanocrystals (NCs) are a class of benign semiconductors that show size and composition-tunable energy gaps and promising optical properties because of the lattice disorder. The random distribution of elements within the alloys can lead to efficient light–matter interactions, making them attractive for Si-compatible optoelectronic devices, transistors, charge storage, and memory applications. However, the fabrication of discrete, quantum-confined alloys has proved a challenging task. Herein, we report solid-state co-disproportionation of a hydrogen silsesquioxane (HSQ)/GeI₂ composite precursor to produce homogeneous Si₁₋ₓGeₓ NCs with control over the diameter (5.9 ± 0.7–7.8 ± 1.1 nm) and composition (x = 0–14.4%) with strong size confinement effects and visible to near IR absorption and emission properties. As-synthesized alloys show an expanded diamond cubic Si structure, a systematic red-shift of Si–Si Raman peak, and emergence of Si–Ge/Ge–Ge peaks with increasing Ge, consistent with the admixture of isovalent elements. Surface analysis of alloys reveals Si⁰/Ge⁰ core and Siⁿ⁺/Geⁿ⁺ surface species and efficient surface functionalization with alkyl ligands *via* thermal hydrosilylation and/or hydrogermylation. Alloy NCs exhibit absorption onsets (2.26–1.92 eV), indirect (1.53–1.80 eV) and direct (2.88–2.47 eV) energy gaps, and photoluminescence (PL) maxima (1.40–1.27 eV) that can be tuned by manipulating the diameter and/or composition. The experimental PL energies are consistent with those predicted by density functional theory (DFT), suggesting that the PL originates from NC core electronic transitions. The facile low-temperature solid-state synthesis and control over physical properties realized in this study will allow discrete Si₁₋ₓGeₓ NCs to emerge as low to nontoxic, earth-abundant, and Si-compatible nanostructures for a broad range of electronic and photonic technologies.

[a]*Department of Chemistry, Virginia Commonwealth University, Richmond, Virginia 23284-2006, USA. E-mail: iuarachchige@vcu.edu*
[b]*Department of Electrical and Computer Engineering, Virginia Commonwealth University, Richmond, Virginia 23284-9052, USA*

†Electronic supplementary information (ESI) available. See DOI: https://doi.org/10.1039/d4nr03472d

Introduction

Semiconductor nanostructures are a promising class of materials that show size- and morphology-tunable optical properties leading to potential applications in solar cells,[1–3] light-emitting diodes,[4,5] photodetectors,[4] and bioimaging[5–7] and sensing[8,9] technologies. Although direct-gap semiconductors such as Cd and Pb chalcogenides, In and Ga arsenides, and lead halide perovskites have shown promise in optical studies due to their efficient light–matter interactions, the inherent high toxicity of these materials impedes their widespread applications. Consequently, interest has shifted towards potentially benign semiconductor systems such as Si and Ge owing

to their low to non-toxicity, high natural abundance, and excellent compatibility with complementary metal oxide semiconductor (CMOS) technology.[10–13] Unfortunately, a disadvantage of Si and Ge-based systems is their indirect band structure which severely limits light–matter interactions compared with those of direct-gap semiconductor counterparts.[14,15] However, this drawback can be resolved by creating materials in the quantum-confined regime because of the removal of translational symmetry, eliminating the momentum-dependence of energy bands, and instigating a substantial increase in optical efficiency.

Synthesis of Si nanostructures with tunable optical properties has gained considerable interest since the first observation of photoluminescence (PL) from porous Si and the high sensitivity of its electronic structure to dopants and surface properties.[16,17] Although quantum confinement has been shown to tune the optical properties of Si NCs by manipulating their diameter, the upper size threshold for confinement effects is not accurately known, and the data correlating size *vs.* PL energy vary widely, with minimum correlation with each

other.[18–21] In cases where size-tunable PL was noted, only a narrow range of NC sizes and thus PL energies was reported.[18,22] Moreover, the core emission of Si NCs appears to be influenced by the fundamental indirect-gap of the bulk material, displaying large Stokes shifts, broad PL line widths, and long PL lifetimes (up to ~100 μs), despite the confinement-induced direct-gap behavior.[23–27] Admixing of other Group IV elements (Ge and Sn) can be utilized to overcome size *vs.* absorption/PL tunability limitations and produce quantum-confined alloy NCs with size and/or composition-tunable PL properties. For instance, our group and others demonstrated the colloidal synthesis and optical characterization of $Ge_{1-x}Sn_x$ [28–31] and $Ge_{1-x-y}Si_ySn_x$ [32] alloy NCs that show size and composition-tunable optical properties across the visible to near IR spectrum. The admixture of Sn into Si and Ge nanostructures also increases the oscillator strengths of optical transitions,[33] producing alloys with enhanced optical properties. Although $Ge_{1-x}Sn_x$ alloys have been reported in several studies, only a handful of reports on $Si_{1-x}Sn_x$ alloys are known because of their larger difference in lattice constants (17.31%).[15,34] Accordingly, Sn has been employed in Si-based systems as a seed element for the promotional growth of anisotropic Si nanostructures.[13,35,36] In contrast to tetragonal Sn, cubic Ge exhibits complete miscibility with Si owing to their comparable lattice parameters and identical crystal structures.[37,38] Homogeneous alloying of Si and Ge will widen the absorption/PL energy range, allowing for fine tuning of optical properties by manipulating the size and/or composition. Moreover, increased disorder in the $Si_{1-x}Ge_x$ alloy has been proposed to augment light–matter interactions, leading to improved molar absorptivities, radiative rates, and PL efficiencies.[39,40]

Although several theoretical[41–43] and experimental[40,44–47] studies of $Si_{1-x}Ge_x$ nanostructures are reported, the synthesis of quantum-confined alloys has proved to a challenging task. To date, $Si_{1-x}Ge_x$ NCs have been produced by molecular beam epitaxy (MBE),[48] co-sputtering,[40] nonthermal plasma pyrolysis,[49] and thermal disproportionation of siloxane–germoxane suboxides.[47] Despite the composition-tunable PL achieved, these methods admit to several drawbacks including Ge segregation, poor size and shape control, and the creation of alloy NCs embedded in a matrix. Moreover, $Si_{1-x}Ge_x$ NCs were also produced *via* disproportionation of a commercial hydrogen silsesquioxane (HSQ)-GeI₂ precursor, where Si- and Ge-rich NCs were obtained in lieu of a homogeneous alloy.[49,50] To our knowledge, the synthesis of discrete, homogeneous $Si_{1-x}Ge_x$ alloy NCs and systematic elucidation of optical properties as a function of size and composition has not been reported. This can be attributed to the limitation of techniques available for homogeneous alloy growth, which require extreme conditions and expensive equipment.[51–53] Recently, thermal disproportionation of an HSQ precursor with a cage-like network structure has been reported to produce size-tunable Si NCs avoiding intricate procedures.[18,54] A low-cost alternative to cage-HSQ that adopts a polymeric network-structure (polymer-HSQ) has also been used in the synthesis of Si NCs.[20] The NCs obtained from polymer-HSQ exhibit similar characteristics to those obtained from cage-HSQ but require a lower disproportionation temperature for NC growth.[19,21,55–57] The incorporation of Ge could further decrease the growth temperature due to Ge seeds acting as nucleation sites for homogeneous alloy growth.

Herein, we report the synthesis of phase pure, homogeneous $Si_{1-x}Ge_x$ alloy NCs with narrow size dispersity (5.9 ± 0.7–7.8 ± 1.1 nm) and tunable composition (x = 0–14.4%) *via* low-temperature thermal disproportionation of an HSQ polymer/GeI₂ composite precursor. HF etching and subsequent hydrosilylation/hydrogermylation allowed the isolation of discrete NCs surface-passivated with dodecyl ligands. As-synthesized alloys display a systematic expansion of diamond cubic Si structure along with a red-shift of the Si–Si Raman peak and emergence of Si–Ge/Ge–Ge peaks with increasing Ge. The oxidation states of core- and ligand-bound Si and Ge species suggest efficient passivation of the NC surface with alkyl ligands. The alloy NCs show strong size confinement effects and composition-tunable absorption onsets and PL peak maxima from 2.26–1.92 eV and 1.40–1.27 eV, respectively, for x = 0–14.4% compositions. The energy gaps estimated from the PL spectra are consistent with those predicted by density functional theory (DFT), suggesting that PL originates from core electronic transitions as opposed to the high-energy, surface-related PL peaks often observed for single-element Si and Ge nanostructures.

Experimental

Materials

Trichlorosilane (99%) was purchased from Sigma Aldrich. GeI₂ was purchased from Richard Blair's laboratory (University of Central Florida) and used without any further purification.[58] 1-Dodecene (96%) and hydrofluoric acid (48–51%, in water) were purchased from Thermo Scientific. Common solvents such as methanol (99+%), ethanol (95%), ethyl acetate (99.5+%), and toluene (99.5%) were ACS grade and purchased from Fisher Scientific or Acros. Organic solvents were dried under molecular sieves (ethanol and methanol) or Na (toluene) before being distilled under nitrogen prior to use. 1-Dodecene was degassed with the freeze–pump–thaw method and stored under nitrogen prior to use. 18 MΩ Milli-Q filtered water was used in all syntheses.

Synthesis of GeI₂/hydrogen silsesquioxane (HSQ) composite precursor

Polymer-HSQ was prepared by following a method reported in the literature.[20] Under a nitrogen atmosphere, 80 mL of methanol was added to a 250 mL flask. This flask was submerged in an ice bath before 4.5 mL of HSiCl₃ was added while the temperature was maintained below 15 °C. Under rapid stirring, 18 mL of Milli-Q filtered water was rapidly injected into the flask, which caused an increase in temperature to ~35 °C. Then, the mixture was allowed to stir for 2 h during which a white jello-like gel is formed. After stirring, the gel was vacuum filtered and washed three times with methanol to

remove any residual water. It should be noted that for the synthesis of $Si_{1-x}Ge_x$ alloy NCs, the polymer-HSQ precursor should not be fully dried, to preserve the porous, jello-like structure of the gel. For the synthesis of Si NCs, the synthesis procedure of polymer-HSQ was kept the same, but it was allowed to fully dry under vacuum for 14 h.

In a separate flask, an appropriate amount of GeI_2 (ESI, Table S2†) was combined with 40–80 mL of methanol under nitrogen. This mixture was rapidly stirred for 1 h to fully dissolve the GeI_2. Then, the partially dried polymer-HSQ was added to the GeI_2/methanol solution under rapid stirring and the mixture was stirred for another 1 h to ensure homogeneous mixing of both components, and the chunks of HSQ gel are thoroughly broken up. After 1 h, the solution was transferred to a rotary evaporator where the methanol was removed under vacuum. As-synthesized HSQ/GeI_2 composite precursor was fully dried under vacuum for ~12 h.

Synthesis of Si and $Si_{1-x}Ge_x$ alloy NCs embedded in a silica matrix

For the synthesis of Si NCs, 500 mg of polymer-HSQ precursor was placed in a quartz boat and loaded into a tube furnace containing a quartz tube. The furnace was heated to 1100 °C at a heating rate of 7 °C min^{-1} and held there for 4 h under an Ar/H_2 (95%/5%) atmosphere. After annealing, the furnace was controllably cooled at a rate of 2 °C min^{-1} until 25 °C was reached. Likewise, $Si_{1-x}Ge_x$ alloy NCs embedded in a silica matrix were produced through a simultaneous disproportionation of polymer HSQ/GeI_2 composite precursor.[50] In a typical synthesis, 500 mg of the composite was placed in a quartz boat and loaded into a tube furnace containing a quartz tube. The furnace was heated to 600 °C at a heating rate of 18 °C min^{-1} and held there for 1 h under Ar/H_2 (95%/5%). Then, the furnace was controllably cooled at a rate of 2 °C min^{-1} until 25 °C was reached.

Liberation of Si and $Si_{1-x}Ge_x$ alloy NCs from the silica matrix

Caution: HF is extremely hazardous and must be used in accordance with local regulations! Used HF solutions must be neutralized in a solution of $CaCl_2$ before being disposed of as acidic waste. Si NCs embedded in silica were ground in a mortar and pestle until a fine powder was achieved. 500 mg of annealed/powdered HSQ was transferred to a polypropylene tube and suspended in 5 mL of ethanol and water. Etching was performed by mixing with 5 mL of aqueous HF. The concentration of the HF etch solution was approximately 25%. This mixture was stirred for 1 h under a N_2 atmosphere to liberate the H-functionalized Si NCs from the silica matrix. Then, 15 mL of toluene was added to the above solution and this gently shaken to extract the H-coated Si NCs. The top toluene layer was transferred into a clean polypropylene tube before being centrifuged for 5 min to form an NC pellet. The clear, colorless supernatant was decanted, and the H-functionalized Si NCs were suspended in 1-dodecene.

A slightly modified procedure was adopted for the isolation and purification of $Si_{1-x}Ge_x$ alloy NCs. The alloy NCs embedded in silica were ground in a mortar and pestle until a fine powder was achieved. 500 mg of this powder was transferred to a polypropylene tube and suspended in 3.5 mL of ethanol. Etching was performed by adding 10 mL of aqueous HF under nitrogen to liberate H-terminated $Si_{1-x}Ge_x$ NCs. This suspension was stirred for 16–48 h, depending on the nominal $Si_{1-x}Ge_x$ composition used in the synthesis (ESI, Table S2†). After etching, 15 mL of toluene was added and the mixture was gently shaken to extract the alloy NCs. The top toluene layer was transferred into a clean polypropylene tube before being centrifuged for ~10 min. The clear, colorless supernatant was decanted and the alloy NCs were suspended in 1-dodecene.

Surface functionalization of Si and $Si_{1-x}Ge_x$ alloy NCs *via* hydrosilylation and/or hydrogermylation

The suspension of $Si_{1-x}Ge_x$ alloy NCs in 1-dodecene was transferred into a three-neck flask and attached to a Schlenk line. Then, the flask was purged with nitrogen for 5 min, heated to 190 °C, and refluxed for 6 h. A similar procedure was used for the hydrosilylation of Si NCs; however, the particles were refluxed at 190 °C for 12 h.

Fractionation, isolation, purification, and size-selective precipitation of $Si_{1-x}Ge_x$ alloy NCs

After hydrosilylation and/or hydrogermylation, the dodecyl-coated $Si_{1-x}Ge_x$ NC solution was centrifuged at 6000 rpm for 5 min to separate the bulk-like, colloidally unstable particles from the colloidally stable alloy NCs. The supernatant containing colloidally stable $Si_{1-x}Ge_x$ NCs was decanted into a separate centrifuge tube. Then, 40 mL of ethanol was added, forming two layers where the top layer contained 1-dodecene and NCs and the bottom layer contained ethanol and ~5 mL of 1-dodecene. Then, the solution was centrifuged at 6000 rpm for 5 min and the clear, bottom layer was pipetted off. This process was repeated, and after the second addition of ethanol, the ethanol and 1-dodecene layer became miscible, allowing the NCs to form a pellet at the bottom of the tube after centrifugation. The clear supernatant was decanted, and 3 mL of ethyl acetate and 0.5 mL of ethanol was added to remove any residual ligands. This suspension was centrifuged at 6000 rpm for 5 min and the clear supernatant was decanted. Then, the NC pellet was dispersed in 3 mL toluene and centrifuged at 6000 rpm for 5 min to isolate colloidally stable NCs. Finally, size-selective precipitation was used to improve the size dispersity of the NCs.[59,60] The supernatant containing $Si_{1-x}Ge_x$ NCs was transferred to a new centrifuge tube and 20–30 drops of methanol were slowly added until the solution turns cloudy. This solution was centrifuged at 6000 rpm for 5 min and the supernatant, considered fraction 2, was transferred to a new centrifuge tube. Fraction 1 is considered to be the pellet at the bottom after centrifugation which was used in XPS studies along with fraction 2. Fraction 2 was kept in solution or dried under vacuum and was considered the final product used in all characterization studies unless otherwise specified. The colloidally unstable $Si_{1-x}Ge_x$ NCs, fraction 1, were resuspended in 3 mL

of toluene and 3 mL of methanol before being centrifuged at 6000 rpm for 5 min to purify the unstable NCs. This process was repeated one more time. Si NCs were also purified through the same procedure. No fractionation or size-selective precipitation was attempted for Si NCs.

Physical characterization of Si and $Si_{1-x}Ge_x$ alloy NCs

Bright-field transmission electron microscopy (TEM) images were recorded with a Zeiss model Libra 120 electron microscope operating at 120 kV. High resolution TEM (HRTEM) and high angle annular dark field (HAADF) images, and selected area electron diffraction (SAED) patterns were recorded using a JEOL JEM-F200 cold FED electron microscope operating at 200 kV. d-Spacings derived from HRTEM were calculated in ImageJ by plotting the inverse FFT images of NCs. d-Spacings derived from SAED were computed in ImageJ by drawing an ellipse around the (111) diffraction pattern to obtain the radius. NC diameters were measured using ImageJ from bright-field TEM images. For spherical and oblong alloy NCs, the average diameter was measured along the longest axis. TEM grids were prepared by drop-casting a dilute solution of NCs in toluene onto an ultrathin carbon film on a lacey carbon copper grid (Ted Pella). An energy dispersive X-ray spectroscopy (EDS) device connected to an SEM operating at 10 keV was used to determine the experimental composition of all samples. The NCs were placed on a double-sided carbon tape attached to an aluminum sample holder and compositions were averaged from five different spots across the sample. Powder X-ray diffraction (PXRD) patterns were recorded using a PANalytical powder X-ray diffractometer equipped with a Cu Kα (λ = 1.5418 Å) radiation and calibrated with a Si standard. Crystallite sizes were calculated using the Scherrer formula.[61] d-Spacings derived from PXRD were computed using the (111) peak. Lattice parameters were calculated using (111), (220), and (311) diffraction peaks and the averaged values are reported. Raman spectra were recorded using a Thermo Scientific DXR Raman spectrophotometer equipped with a 532 nm laser. Fourier Transform Infrared Spectroscopy (FTIR) was recorded using a Thermo iS50 FTIR. XPS spectra were recorded using a Thermo Fisher model ESCALAB 250 XPS instrument with an Al Kα radiation source. X-ray photoelectron spectroscopy (XPS) spectra were recorded with a source wavelength of 1486.6 eV, a pass energy of 26 eV, and a step rate of 0.1 eV. XPS peaks in the Si and Ge regions were calibrated using the C(1s) peak at 284.8 eV and the spectral deconvolution and peak analyses were performed using MultiPak software, which takes into account the spin–orbit coupling.

Optical characterization of Si and $Si_{1-x}Ge_x$ alloy NCs

Solid-state diffuse reflectance spectra of alloy NCs were recorded using an internal diffuse reflectance DRA 2500 attachment and a $BaSO_4$ background holder in a Cary 6000i UV-Vis-near IR spectrophotometer (Agilent Technologies). Tauc analysis with multiline piecewise fitting was performed as described in previous publications,[56] with average R^2 values of 0.997 (indirect) and 0.987 (direct). Room-temperature PL

spectra of the drop-cast samples were measured with ~10 W cm^{-2} 405 nm continuous excitation (Coherent Obis) by liquid nitrogen-cooled Princeton Instruments CCD and InGaAs detectors mounted onto a 30 cm focal length spectrograph. PL spectra were filtered to remove the remaining excitation contribution and were corrected for the standard spectral response of the measurement system obtained *via* quartz tungsten halogen (QTH) and Hg(Ar) calibration lamps. Peaks were determined through bi-Gaussian fitting, with an average R^2 value of 0.998.

Computational energy gap calculations of Si, Ge, and $Si_{1-x}Ge_x$ alloy NCs

The raw geometry of $Si_{1-x}Ge_x$ NCs with x = 0.00, 0.05, 0.10, 0.15, 0.20, 0.35, and 1.00 were generated using the Python module ASE.[62] For NCs containing a specific composition, the desired Ge concentration was achieved through random swapping of Si atoms with Ge atoms. To mitigate heavy computing costs, the open bonds at the surface of each NC were capped with hydrogens. Si-based NCs with four different sizes were produced: 1.4 nm (134 atoms), 1.8 nm (240 atoms), 2.1 (402 atoms), and 2.4 nm (444 atoms). It should be noted that the standard algorithm for DFT scales used at least the cube of the system size, limiting routine calculations to systems comprising only a few hundred atoms without relying on a supercomputer. Thus, the first-principles studies of NCs in this work were focused on systems up to 444 atoms, which are much larger than model systems typically consisting of fewer than one hundred atoms in the literature, pushing the boundary of computational studies to real systems. For each size and dopant concentration, a total of three NCs were generated to minimize the impact of the random distribution of Ge atoms, with the resulting value being averaged. The SPW92/def2-SVP method was utilized to optimize the NC structures due to its reliable performance in reproducing experimental lattice constants, as demonstrated in our prior studies.[11] Subsequently, based on the SPW92/def2-SVP optimized NC structures, the energy gaps were calculated using HLE16/CRENBL, which was also employed in our previous studies.[11] Additionally, for 2.1 nm pure Ge and Si NCs, HLE16/CRENBL produced energy gaps of 2.5 and 3.1 eV, respectively. These results are consistent with previous computational findings of 2.5 eV for pure Ge NCs and 2.5–3.5 eV for pure Si NCs with a similar diameter,[33,63–65] indicating the reliability of HLE16/CRENBL for energy gap calculations. Finally, a power law curve was fitted using HLE16/CRENBL//SPW92/def2-SVP calculated gaps against NC size for each Ge concentration. To ensure the asymptotic decay toward the bulk gap value at larger sizes, the band gap energies for all curves between 11.7 to 12 nm at a 0.01 nm interval as bulk values were obtained, using the following experimental model for bulk, with x representing the percent Ge and $E_{g, infinity}$ as the gap for bulk.[38,66–68]

$$E_{g,infinity} = 2.010 - 1.270(1 - x) \quad \text{if} \quad x < 0.15$$

$$E_{g,infinity} = 1.155 - 0.43(1 - x) + 0.206(1 - x)^2 \quad \text{if} \quad x > 0.15$$

Results and discussion

Although matrix-embedded $Si_{1-x}Ge_x$ NCs have been produced by induced pyrolysis, thermal evaporation, co-sputtering, and nonthermal plasma methods,[40,50,69–71] the synthesis of discrete, colloidally stable, and quantum-confined alloys with variable composition has not been reported. While $Si_{1-x}Ge_x$ alloys are thermodynamically stable over a wider temperature range, Si typically requires high (≥800 °C) temperatures to crystallize. In addition, Si is prone to oxidation, impelling most of the published literature studies to produce Si and $Si_{1-x}Ge_x$ NCs encased in a SiO_2 matrix or allow minor surface oxidization as a form of natural surface passivation.[37,40,68,70] However, surface coordination of oxygen has been shown to alter the optical properties of Group IV NCs, emphasizing the need for proper passivation for the elucidation of size and composition-dependent physical properties.[72–74] Hence, the use of an HSQ polymer-based synthetic route offers a favorable silica matrix for $Si_{1-x}Ge_x$ NC growth, crystallization, and alloying. Although early success has been reported with the synthesis of $Si_{1-x}Ge_x$ NCs using GeI_2 due to its disproportionation temperature (~330 °C) being in the same range as HSQ (250–450 °C), extensive Ge segregation and sample heterogeneity have also been reported.[49,50] Complexing agents such as alkylphosphines were used to disperse GeI_2 and HSQ in a common solvent (methyl isobutyl ketone) and form a composite precursor; however carbon/phosphorus contamination is possible. In our studies, we found that GeI_2 can be sufficiently incorporated into polymer-HSQ by suspending it in methanol, and precipitating the HSQ/GeI_2 composite *via* evaporation of methanol. The low boiling point of methanol allows complete removal under vacuum, ensuring no carbon-based impurities are retained in the HSQ/GeI_2 composite. Subsequent thermal disproportionation of the composite at relatively low temperature (~600 °C) was used to produce phase pure $Si_{1-x}Ge_x$ alloy NCs.

Unlike colloidal NC synthesis routes that utilize relatively low temperatures and homogeneous precursor solutions, Ge segregation in an inherently heterogeneous solid-state synthetic route is possible. To achieve phase pure, homogeneous $Si_{1-x}Ge_x$ alloys, four reaction parameters were taken into consideration: disproportionation temperature and time, etching time, and efficiency of surface passivation. Compared with single-element Si NCs, a lower annealing temperature and a shorter growth time were required to produce $Si_{1-x}Ge_x$ NCs while elevated temperatures and longer growth times caused local segregation of Ge. The low temperature required for alloy NC growth can be traced back to early *in situ* generation of Ge "seeds". GeI_2 can produce Ge atoms earlier in the annealing process than Si atoms are produced from HSQ because of the differences in the disproportionation temperatures of GeI_2 and HSQ (330 *vs.* 400 °C).[54,75] Hence, Ge seeds can act as nucleation sites for Si, decreasing the temperature required for the crystallization and growth of homogeneous alloys (600 °C) compared with single-element Si NCs (1100 °C).[18–20] This Ge-facilitated growth of $Si_{1-x}Ge_x$ NCs is expected to follow a similar mechanism to that reported for the Sn-induced growth of Si nanostructures where the annealing temperature has been dramatically reduced by the existence of pseudo Ge and/or Sn promoters.[13,35,76] HF etching when performed under ambient light, increases the etch rate due to the creation of photoexcited holes.[77–79] Thus, etching in ambient light along with extended etch times (16–48 h) were used to control the diameter of $Si_{1-x}Ge_x$ NCs and eliminate segregated Ge seeds.[54,78,79]

To produce homogeneous alloys, reaction parameters such as temperature and time should be tuned to achieve the most efficient alloying with no growth of larger, heterogeneous NCs. Hence, HAADF images and scanning TEM (STEM)-energy dispersive spectroscopy (STEM-EDS) elemental maps were recorded to investigate the homogeneity of NCs produced at variable temperatures and growth times (Fig. 1, ESI, Fig. S2†). Similar to single-element Si NCs, the disproportionation temperature can be tuned to control the size and size dispersity of $Si_{1-x}Ge_x$ alloys. As the disproportionation temperature increased from 600 to 800 °C, the size and size dispersity of alloys increased from 7.8 ± 0.8 to 9.8 ± 2.1 nm (Fig. 1J–L, ESI, Fig. S2D†). The average Ge composition is also higher, ~8 *vs.* ~12% Ge, for NCs produced at 600 and 800 °C, respectively. Although an increase in Ge content was observed at higher temperatures, heterogeneous segregation was evident in NCs produced at 800 °C (Fig. 1J–L, ESI, Fig. S2D†), which is consistent with prior reports of $Si_{1-x}Ge_x$ NCs.[80–82] To avoid segregated Ge and decrease the NC size for higher confinement effects, a lower disproportionation temperature (600 °C) was explored in all syntheses. The size and dispersity of alloys can also be controlled by manipulating the growth time at 600 °C (Fig. 1A–I, ESI, Fig. S2A–C†).[18] For instance, alloy NCs produced at 600 °C for 1 h produced homogeneous NCs with x = 6–7% from a 15% nominal Ge sample with spherical to oblong morphology and narrow size dispersity (Fig. 1A–C, ESI, Fig. S2A†). Similarly, alloys produced at 600 °C for 4 h display x = 7–8% compositions, although a less defined morphology was observed (Fig. 1D–F and ESI, Fig. S2B†). Similar to single-element Si NCs, an increase in growth time from 1 to 4 h caused an increase in size and dispersity of the alloys (7.8 ± 0.8 nm to 8.2 ± 1.7 nm, respectively).[83] In contrast, the NCs produced at 600 °C for 7 h were significantly larger and polydisperse (8.6 ± 2.7 nm). Although a higher Ge (x = 8–10%) content has been achieved with 600 °C/7 h reaction, Ge segregation was evident (Fig. 1G–I, ESI, Fig. S2C†). Likewise, Ge segregation was observed in all samples produced above 800 °C (Fig. 1J–L, ESI, Fig. S2D†). Accordingly, the 600 °C/1 h reaction was chosen as the optimal temperature and time for the synthesis of phase pure, homogeneous $Si_{1-x}Ge_x$ NCs.

Bright-field TEM images were recorded to further investigate the morphology and crystallinity of $Si_{1-x}Ge_x$ alloy NCs (Fig. 2, ESI, Fig. S3 and 4†). All samples display discrete, spherical to oblong shaped particles with an average size ranging from 5.9 ± 0.7–7.8 ± 1.1 nm, which are larger than single-element Si NCs produced at 1100 °C (ESI, Fig. S5†). The diameters of the alloys were maintained within a narrow range by manipulating the etching times under ambient light and
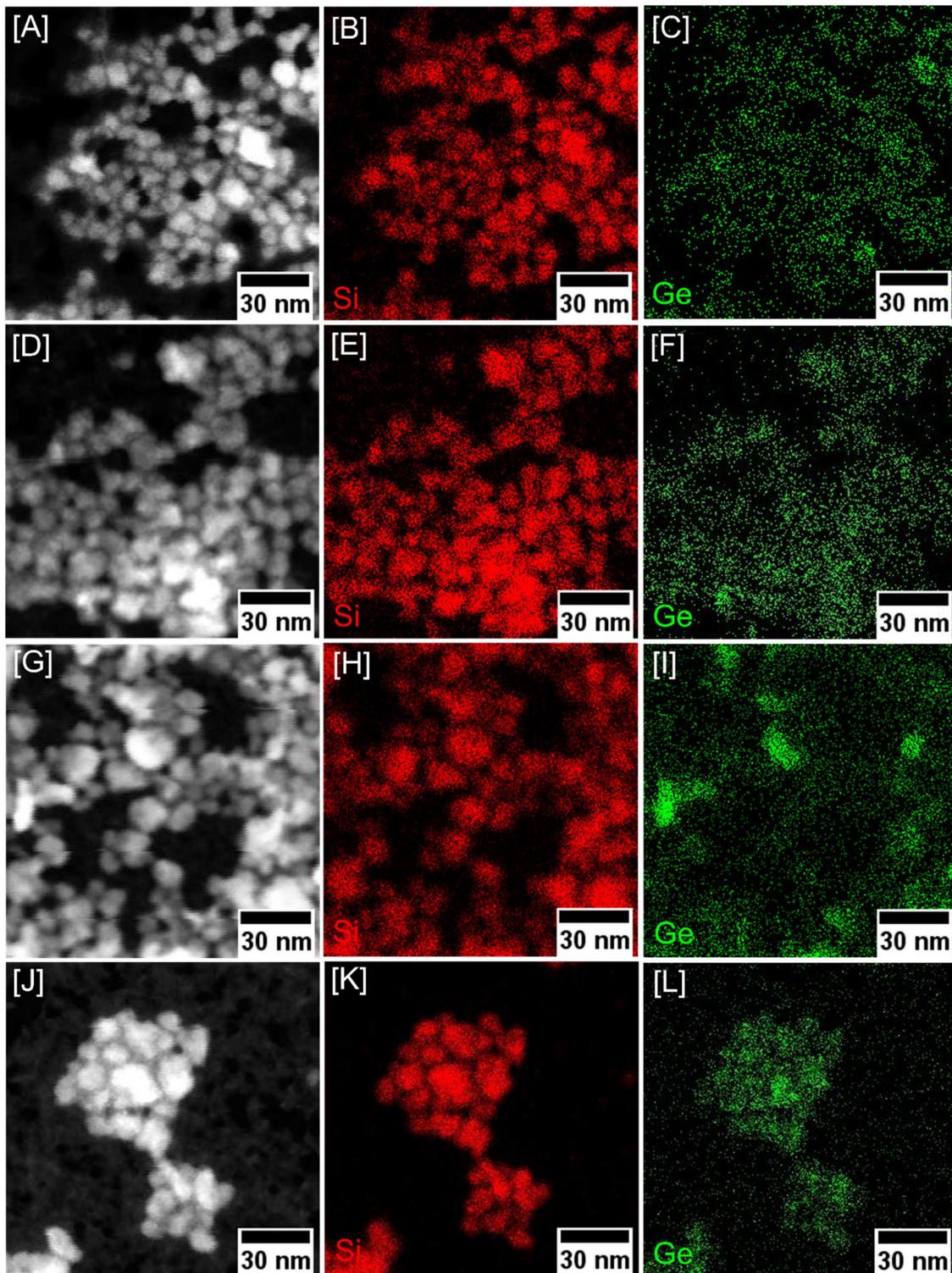
Fig. 1   [A, D, G and J] STEM images and corresponding [B, E, H and K] Si and [C, F, I and L] Ge maps of $Si_{1-x}Ge_x$ NCs produced at variable disproportionation temperatures and growth times: [A–C] $Si_{0.915}Ge_{0.085}$ NCs produced at 600 °C for 1 h, [D–F] $Si_{0.905}Ge_{0.095}$ NCs produced at 600 °C for 4 h, [G–I] $Si_{0.913}Ge_{0.087}$ NCs produced at 600 °C for 7 h, and [J–L] $Si_{0.864}Ge_{0.137}$ NCs produced at 800 °C for 3 h. Corresponding overlays are shown in ESI, Fig. S2.†

size-selective precipitation. All compositions exhibited similar morphology and size control to those of single-element Si NCs produced by similar methods.[20,57] Interestingly, there is an

upper composition limit (~15% Ge) for size and morphology control. Above this limit, the average diameter decreases whereas the size dispersity increases (ESI, Fig. S4B†). When
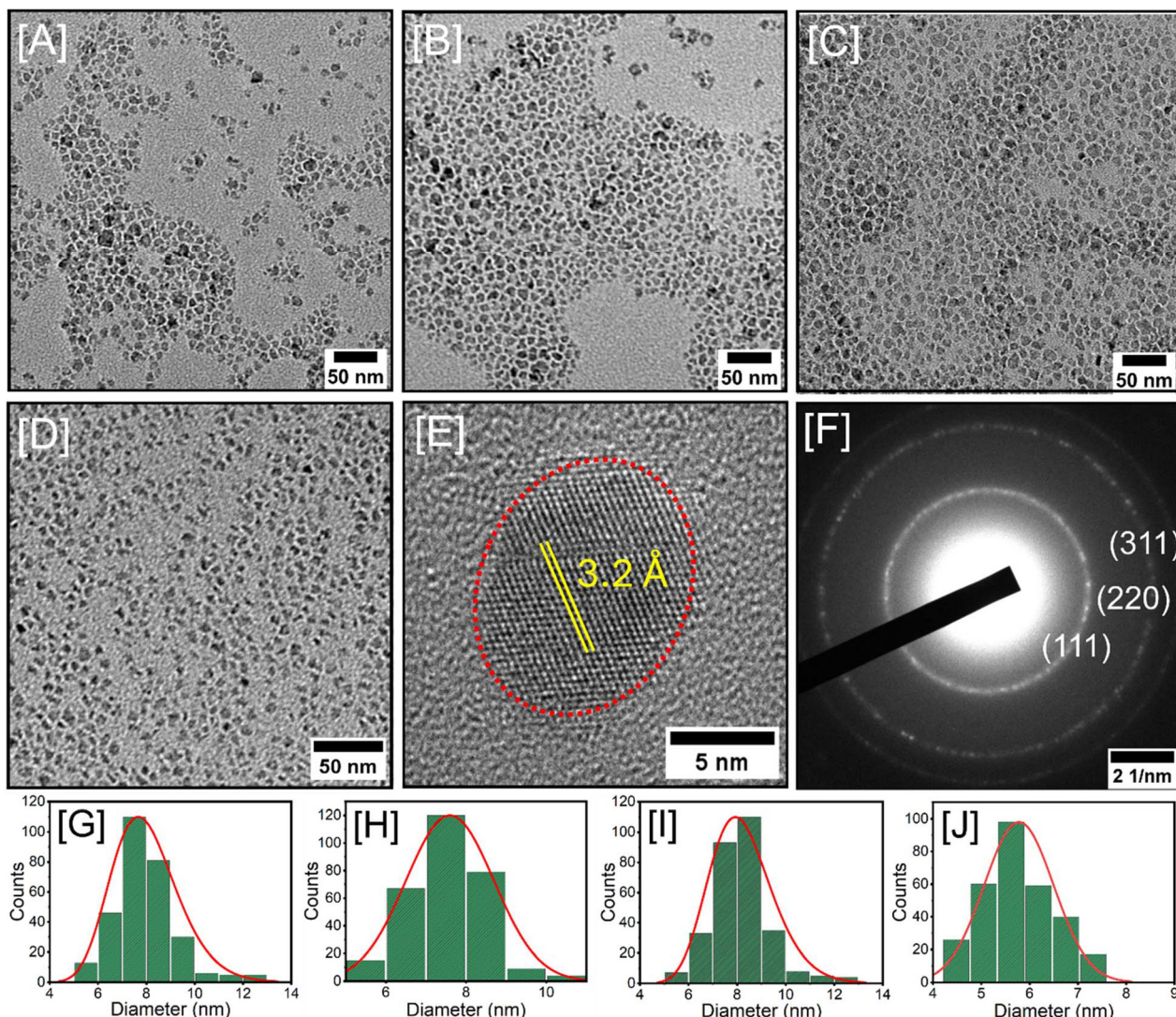
Fig. 2 Representative bright-field TEM images of [A] $Si_{0.988}Ge_{0.012}$, [B] $Si_{0.957}Ge_{0.043}$, [C] $Si_{0.916}Ge_{0.084}$, and [D] $Si_{0.884}Ge_{0.116}$ alloy NCs along with [E] HRTEM image of $Si_{0.944}Ge_{0.056}$ NCs displaying the (111) lattice spacing. [F] A representative SAED pattern of $Si_{0.916}Ge_{0.084}$ NCs. Size histograms of [G] $Si_{0.988}Ge_{0.012}$, [H] $Si_{0.957}Ge_{0.043}$, [I] $Si_{0.916}Ge_{0.084}$, and [J] $Si_{0.884}Ge_{0.116}$ alloy NCs. Size histograms of other compositions are included in ESI, Fig. S6.†
The average diameters and d-spacings of alloys are shown in Table 1 and ESI, Table S1,† respectively.

the Ge content is >14.4%, size control is greatly diminished, resulting in less morphologically defined aggregates of NCs (ESI, Fig. S4C†). This phenomenon was also seen in the HSQ polymer system when Sn has been employed as a nucleation seed that prompted the growth of anisotropic Si nanostructures in lieu of spherical NCs.[13] Similar results have also been reported with the solution synthesis of $Ge_{1-x}Sn_x$ alloy NCs where Sn acts as a promoter for NC growth.[84,85] To confirm lattice expansion due to Ge incorporation, d-spacing values were calculated from the HRTEM and SAED patterns shown in Fig. 2F and ESI, Fig. S3, 5, and 7.† Both techniques revealed increased (111) spacings of 3.12–3.14 Å and 3.12–3.16 Å for x = 0–14.4%, respectively (ESI, Table S1†), which are consistent with (111) spacings of bulk Si (3.14 Å) and $Si_{0.850}Ge_{0.150}$ alloys (3.15 Å).[37] Moreover, all compositions

showed discrete alloy NCs indicating successful etching and subsequent hydrosilylation and hydrogermylation with dodecyl ligands (Fig. 3F, G).

To investigate the effects of alloying on structure and crystallinity, PXRD patterns of colloidally stable $Si_{1-x}Ge_x$ NCs were recorded and are shown in Fig. 3A and B. Due to inherently heterogeneous mixing of an insoluble HSQ polymer with a GeI_2/methanol solution, segregation of Ge within the HSQ network is possible. However, as-synthesized alloys show Bragg reflections corresponding to diamond-cubic Si (JCPDS 00-001-0971) without any impurities. Upon alloying with Ge, a shift in diffraction patterns to lower 2θ angles is expected as Ge, a larger atom, expands the Si lattice.[33] Similar to single-element Si NCs, the average diameters of alloy NCs obtained from TEM are larger than the crystallite sizes computed from (111) Bragg
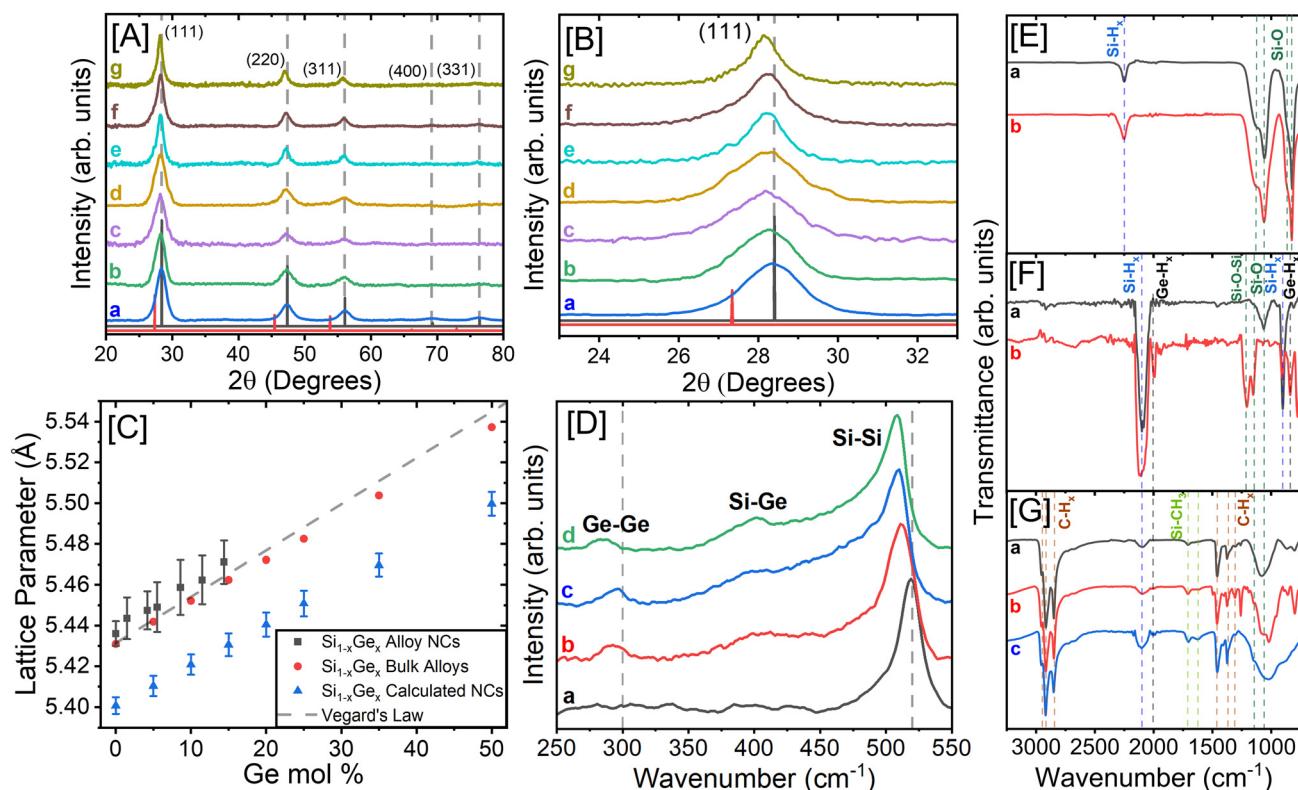
Fig. 3 [A] PXRD patterns of (a) $Si_{1.000}Ge_{0.000}$, (b) $Si_{0.988}Ge_{0.012}$, (c) $Si_{0.957}Ge_{0.043}$, (d) $Si_{0.944}Ge_{0.056}$, (e) $Si_{0.916}Ge_{0.084}$, (f) $Si_{0.884}Ge_{0.116}$, and (g) $Si_{0.856}Ge_{0.144}$ alloy NCs. [B] Corresponding magnified (111) peaks of all compositions. ICCD-PDF overlays of diamond cubic Si (JCPDS 00-001-0971) and Ge (JCPDS 01-89-5011) are shown as vertical black/dashed and red lines, respectively. [C] Average experimental lattice parameters obtained for bulk and nanocrystalline $Si_{1-x}Ge_x$ alloys along with those computed from DFT as a function of composition. [D] Raman spectra of (a) $Si_{1.000}Ge_{0.000}$, (b) $Si_{0.916}Ge_{0.084}$, (c) $Si_{0.884}Ge_{0.116}$, and (d) $Si_{0.856}Ge_{0.144}$ alloy NCs. The dashed lines at 520 cm^{-1} and 300 cm^{-1} represent phonon modes corresponding to bulk Si–Si and Ge–Ge bonds, respectively. FTIR spectra of [E] polymer-HSQ and HSQ/GeI$_2$ precursors used in the synthesis of (a) Si and (b) $Si_{0.600}Ge_{0.400}$ NCs, [F] freshly etched, H-terminated (a) Si and (b) $Si_{1-x}Ge_x$ NCs, and [G] dodecyl passivated (a) Si and (b) colloidally stable and (c) unstable $Si_{1-x}Ge_x$ NCs.

reflection (Table 1). The notable difference between the crystallite and average particle size indicates the possible presence of an amorphous layer in alloy NCs.[86] Lattice spacings computed from the (111) peaks are in the range of 3.14–3.17 Å for $x = 0–14.4\%$, consistent with those obtained from HRTEM and SAED (ESI, Table S1†). These data, along with d-spacings obtained from the (220) and (311) peaks (ESI, Fig. S8†) were used to calculate lattice parameters as a function of composition. The computed lattice constants show an increase from 5.4361–5.4711 Å for $x = 0–14.4\%$ compositions (Fig. 3C, black squares and Table S1†). These values are slightly larger than those reported for bulk $Si_{1-x}Ge_x$ alloys (5.4310–5.4624 Å); however, they followed a similar trend with increasing Ge and Vegard's law is generally obeyed. The experimental lattice constants were also compared with those calculated from DFT at the SPW92/def2-SVP level, a method previously demonstrated to reliably reproduce experimental lattice parameters.[32] The SPW92 lattice parameters are underestimated by ~0.03 Å compared with bulk and NC lattice constants (Fig. 3C, blue triangles).[32,87] This underestimation is expected because SPW92 tends to overestimate cohesive energies.[32,87]

Nevertheless, this deviation is marginal, approximately 0.5%, which falls below the 1–2% deviation generally observed among computational and experimental lattice constant values.[88]

PXRD patterns of $Si_{1-x}Ge_x$ NCs encapsulated in the SiO_2 matrix show a large, broad hump at ~22° corresponding to amorphous silica (ESI, Fig. S9a†).[18,89] However, this hump disappears upon HF etching and hydrosilylation/hydrogermylation, suggesting the liberation of free-standing $Si_{1-x}Ge_x$ NCs (Fig. 3A, B, F and G).[54] The sharp peaks observed in $Si_{1-x}Ge_x$/ SiO_2 matrix correspond to Si-rich and Ge-rich $Si_{1-x}Ge_x$ alloy NCs. These particles can be separated from homogeneously alloyed $Si_{1-x}Ge_x$ NCs after HF etching and surface passivation with dodecyl ligands. The colloidally unstable $Si_{1-x}Ge_x$ NCs show two separate peaks (ESI, Fig. S9b†), corresponding to Ge-rich and Si-rich particles with considerably larger crystallites of 11.1 and 8.9 nm, respectively. In contrast, the colloidally stable NC faction exhibits peaks corresponding to $Si_{1-x}Ge_x$ alloys with significantly smaller crystallites (~3.5–6.4 nm). The narrow diffraction peaks suggest that the colloidally unstable fraction contains larger, bulk-like heterogeneously alloyed par-

Table 1 A comparison of elemental composition, crystallite size, average diameters, Si–Si, Si–Ge, and Ge–Ge Raman peak positions, PL maxima, absorption onsets, and direct and indirect energy gaps of Si and $Si_{1-x}Ge_x$ alloy NCs (x = 0–14.4%) along with energy gaps predicted from density functional theory (DFT) with theoretical compositions closer to experimentally measured alloy compositions

Experimental composition[a]	Crystallite size[b] (nm)	Diameter[c] (nm)	Raman peak (Si–Si, Si–Ge, Ge–Ge) (cm^{-1})	PL ± FWHM (eV)	Absorption onset[d] (eV)	Tauc indirect (E_g^{i1})	Tauc direct (E_g^d)	Closest theoretical composition[e]	DFT energy gaps[f] (eV)
$Si_{1.000}Ge_{0.000}$	6.6 ± 0.2	7.2 ± 0.7	519, —, —	1.27 ± 0.22	2.26	1.80	2.88	$Si_{1.000}Ge_{0.000}$	1.43–1.59
$Si_{0.988}Ge_{0.012}$	6.7 ± 0.3	7.8 ± 1.1	518, —, —	1.37 ± 0.28	2.23	1.78	2.85	$Si_{1.000}Ge_{0.000}$	1.34–1.57
$Si_{0.957}Ge_{0.043}$	5.4 ± 0.2	7.3 ± 0.8	516, —, —	1.38 ± 0.31	2.10	1.59	2.69	$Si_{0.950}Ge_{0.050}$	1.39–1.57
$Si_{0.944}Ge_{0.056}$	5.7 ± 0.2	7.2 ± 1.1	514, —, 295	1.40 ± 0.31	2.08	1.68	2.79	$Si_{0.950}Ge_{0.050}$	1.37–1.62
$Si_{0.916}Ge_{0.084}$	7.5 ± 0.3	7.8 ± 0.9	512, 402, 293	1.39 ± 0.38	2.03	1.59	2.58	$Si_{0.900}Ge_{0.100}$	1.31–1.49
$Si_{0.884}Ge_{0.116}$	6.2 ± 0.2	5.9 ± 0.7	509, 401, 295	1.39 ± 0.36	2.07	1.61	2.67	$Si_{0.900}Ge_{0.100}$	1.53–1.75
$Si_{0.856}Ge_{0.144}$	7.3 ± 0.2	6.8 ± 1.5	508, 401, 285	1.36 ± 0.38	1.92	1.53	2.47	$Si_{0.850}Ge_{0.150}$	1.33–1.71

[a] Elemental compositions were obtained from SEM/EDS by averaging five different spots per sample. Corresponding EDS spectra are shown in ESI, Fig. S1.† [b] Crystallite sizes were determined by applying the Scherrer formula to the (111) peak of diffraction patterns using a coefficient modifier of 4/3 to account for nonspherical particles.[61] [c] Average diameters were calculated from 200–250 individual NCs from the TEM images of multiple individually prepared samples. [d] Energy gaps were estimated by extrapolation of the first absorption onset to the intersection point of the baseline. [e] DFT calculations were performed on 1.4 to 2.4 nm alloy NCs with x = 0.00, 0.05, 0.10, 0.15, 0.20, 0.35, and 1.00 compositions. An interpolation scheme, utilizing DFT computational values and experimental bulk values, was used to determine the energy gaps for NCs with variable sizes and compositions. [f] Because of the experimental uncertainties of average diameter of $Si_{1-x}Ge_x$ NCs, computational energy gaps are presented as a range.

ticles that are partially passivated with dodecyl ligands (ESI, Fig. S9b†). This phenomenon of a partial hydrosilylation has also been reported in Si NCs with >6 nm diameter due to faceting of the NC surface, decreasing its surface energy except at the edges and corners.[18,90]

To further elucidate the influence of alloying on the structure and bonding of $Si_{1-x}Ge_x$ NCs, Raman spectroscopy was employed (Fig. 3D). Single-element Si and Ge NCs exhibit Raman peaks from 519–507 and 299–294 cm^{-1} corresponding to Si–Si and Ge–Ge bonds, respectively, which are red-shifted from bulk Si (520 cm^{-1}) and Ge (300 cm^{-1}) due to phonon confinement.[55,91] In contrast, $Si_{1-x}Ge_x$ alloy NCs show prominent peaks from 519–508 cm^{-1} corresponding to Ge-alloyed Si–Si bonds. In addition, a peak corresponding to Si–Ge bonds appears at 402–400 cm^{-1} for $Si_{1-x}Ge_x$ alloys with >8.54% Ge, which progressively arises with increasing Ge content.[32,50] A minor Ge–Ge peak was also noted for $Si_{1-x}Ge_x$ NCs with x > 6.02% composition. The red-shift in the Si–Si phonon mode can be attributed to phonon confinement, inherent in quantum-confined NCs and homogeneous alloying of Si with Ge that produces a longer and weaker Si–Ge bond. Therefore, combined effects of phonon confinement and alloying-induced red-shifting cannot be decoupled. However, the influence of phonon confinement is expected to be similar for $Si_{1-x}Ge_x$ NCs with near-consistent average diameters (5.9–7.8 nm).[55] Hence, the red-shifts in Si peaks observed with increasing Ge can be mainly attributed to the homogeneous alloying of Si with Ge. It can also be seen that alloy NCs exhibit a broader, more asymmetric Si–Si peak compared with single-element Si NCs. This can be attributed to increased lattice disorder upon Ge incorporation.[55] At compositions >8.54% Ge, a new peak appears corresponding to the Si–Ge bonds, which becomes pronounced with increasing Ge in the alloy. Both thin film and bulk $Si_{1-x}Ge_x$ studies report that the Si–Ge peak position and relative intensity are directly pro-

portional to the Ge composition. Thus, the systematic increase in intensity of the Si–Ge peak at higher Ge compositions further supports the successful alloying of Ge into the diamond cubic Si NCs.

The effectiveness of HF etching and subsequent surface passivation with alkyl ligands were evaluated by XPS (Fig. 4A–C and ESI, Fig. S10, 11†). The Si 2p region shows two major peaks for Si and $Si_{1-x}Ge_x$ alloy NCs with the highest Ge composition (*i.e.* $Si_{0.856}Ge_{0.144}$). The binding energy of the lower energy peak, corresponding to Si^0, decreases from 99.42 to 99.23 eV for Si NCs to $Si_{0.856}Ge_{0.144}$ alloy NCs. These Si^0 peaks observed in both samples are consistent with bulk and nanocrystalline Si.[18,19,92] Si and Ge show similar electronegativities (1.90 *vs.* 2.01); therefore a slight shift in the Si^0 peak is expected and observed across variable alloy compositions. The higher energy peak centered at 102.3 eV for Si NCs can be deconvoluted to Si^{2+} (102.1 eV), Si^{3+} (102.9 eV), and Si^{4+} (103.5 eV) species (Fig. 4A). The deconvoluted high-energy peaks of $Si_{0.856}Ge_{0.144}$ NCs show similar results with Si^{2+} (101.5 eV), Si^{3+} (102.4 eV), and Si^{4+} (103.3 eV) species (Fig. 4B). These charged species are attributed to surface Si–C bonds formed during hydrosilylation, suggesting effective surface passivation with dodecyl ligands (Fig. 3F and G).[93–95] A smaller Si^{4+} peak at higher energies indicates that minimal SiO_2 is present in both samples, originated presumably from handling and air exposure. The relative intensity of the Si^0 peak compared with those of Si–C peaks can be used to qualitatively determine the variance of NC diameter.[13] Single-element Si NCs exhibit smaller Si–C peaks compared with Si^0 (Fig. 4A) because of the relatively larger diameter and much narrower size dispersity (7.2 ± 0.7 nm). In contrast, $Si_{0.856}Ge_{0.144}$ NCs display more pronounced Si–C peaks compared with the Si^0 peak because of relatively smaller diameter and increased dispersity of NCs (6.8 ± 1.5 nm). This trend was also seen in larger diameter, colloidally unstable $Si_{0.505}Ge_{0.495}$ NCs where the Si^0/Si–C ratio is slightly higher (ESI, Fig. S11A†).
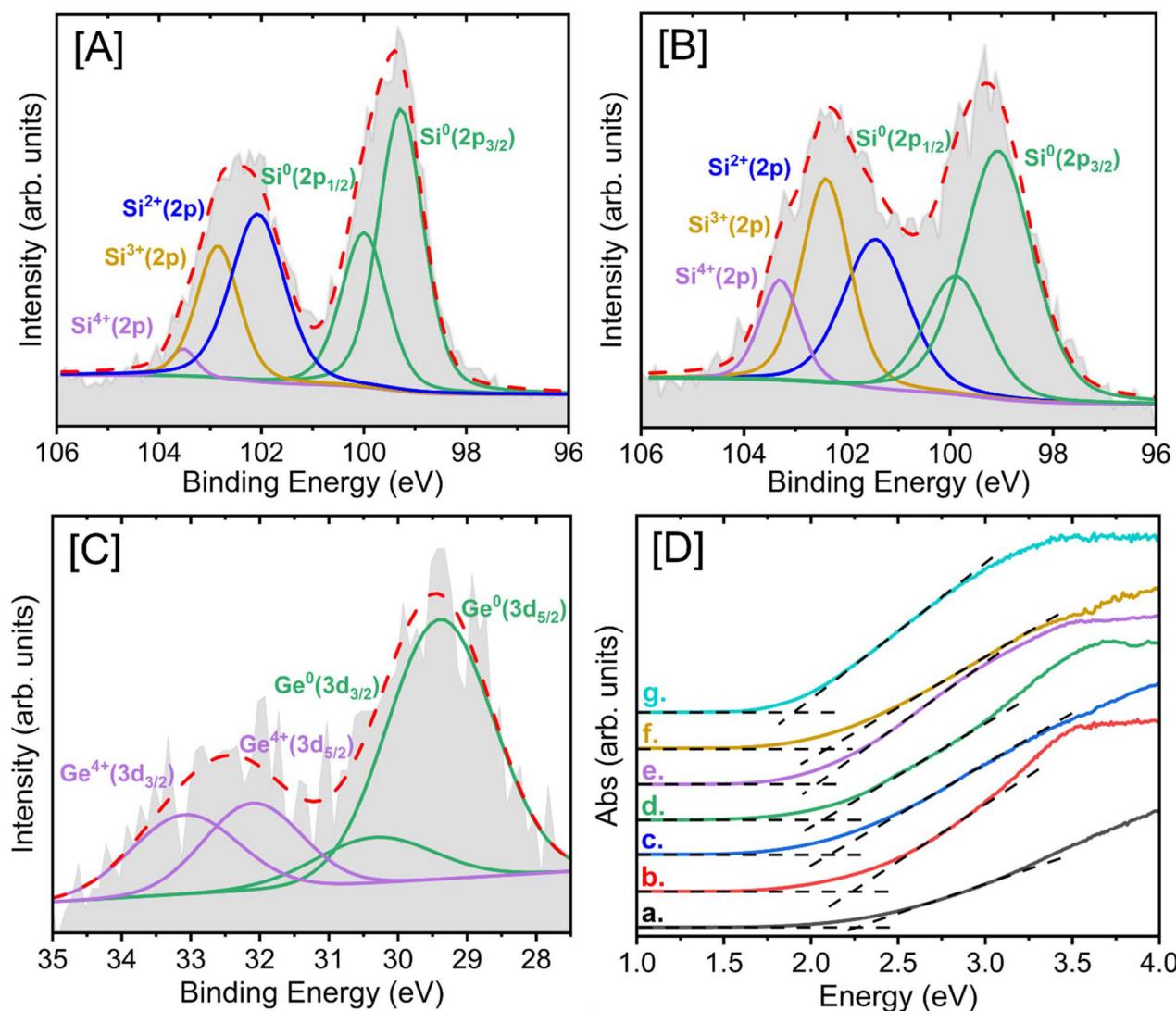
Fig. 4 XPS spectra of [A] the Si 2p region of Si NCs along with the [B] Si 2p and [C] Ge 3d regions of $Si_{0.856}Ge_{0.144}$ alloy NCs. The shaded (semitransparent) plot represents spectral data. The green, blue, tan, and purple lines are fitted peaks for Si^0/Ge^0, Si^{2+} Si^{3+}, Si^{4+}/Ge^{4+} core and surface species, respectively. The red dashed line represents the overall fitted envelope. [D] Solid-state absorption spectra of (a) $Si_{1.000}Ge_{0.000}$, (b) $Si_{0.988}Ge_{0.012}$, (c) $Si_{0.957}Ge_{0.043}$, (d) $Si_{0.944}Ge_{0.056}$, (e) $Si_{0.916}Ge_{0.084}$, (f) $Si_{0.884}Ge_{0.116}$, and (g) $Si_{0.856}Ge_{0.144}$ alloy NCs. The intersections of the dashed lines correspond to the energy gap where a least-squares linear regression analysis was applied. Corresponding absorption onsets are shown in Table 1 and ESI, Table S1.†

Fig. 4C shows the Ge 3d region containing two major peaks corresponding to Ge^0 (29.4 eV) and Ge^{4+} (32.5 eV) species of $Si_{0.856}Ge_{0.144}$ NCs, consistent with the literature.[10,96,97] The broadness of the Ge^0 peak suggests that it can be deconvoluted into a Ge^0 $3d_{5/2}$ (29.3 eV) main peak with a Ge^0 $3d_{3/2}$ shoulder (30.3 eV).[98] The higher energy Ge^{4+} peak (32.5 eV) is likely to originate from small amounts of Ge oxidation indicating a semi-successful hydrogermylation (Fig. 3F and G).[10] In comparison, colloidally unstable, larger $Si_{0.505}Ge_{0.495}$ NCs exhibit a Ge^0 peak located at identical energies (29.3 eV, ESI, Fig. S11B†).[99] These colloidally unstable NCs also show a peak corresponding to Ge^{4+} that can be attributed to small amounts of GeO_2. Similar to Si species, the Ge^0/Ge^{4+} ratio was observed

to increase with larger diameter $Si_{0.505}Ge_{0.495}$ NCs compared with smaller $Si_{0.856}Ge_{0.144}$ NCs due to the higher number of core Ge^0 atoms compared with charged surface species. The high intensity of Ge^{4+} peak suggests a nontrivial amount of surface oxidation affected the overall colloidal stability of larger NCs, explaining why there is a colloidally unstable fraction.

Solid-state diffuse reflectance spectra were recorded to investigate the composition-dependent absorption of $Si_{1-x}Ge_x$ NCs (Fig. 4D and ESI, Fig. S12 and S13†). The reflectance data were converted to absorption using the Kubelka–Munk remission function.[100] Since alloy NCs show consistent average diameters and size dispersity, confinement effects are expected to

be similar across variable compositions. The absorption onsets estimated for 5.9 ± 0.7–7.8 ± 1.1 nm $Si_{1-x}Ge_x$ alloys span from 2.23–1.92 eV for $x = 1.2$–14.4% compositions, respectively, which are red-shifted from single-element Si NCs (2.26 eV) with a 7.2 ± 0.7 nm diameter. The red-shifts observed in $Si_{1-x}Ge_x$ NCs can be attributed to homogeneous admixing of isovalent elements. These onsets are larger and encompass a broader energy range than those reported for bulk and thin film $Si_{1-x}Ge_x$ alloys (1.12–1.02 eV for $x = 0$–15% Ge), consistent with the quantum confinement effects.[38] Additionally, a systematic increase in absorption onsets with increasing Ge content was observed for alloy NCs with similar diameter, further suggesting the successful alloying of Si and Ge.

Absorption properties for $Si_{1-x}Ge_x$ alloy NCs were further explored with direct and indirect gap Tauc analysis (Fig. 6A and ESI, Fig. S13 and S14†). Following closely with Kubelka–Munk derived absorption onsets, primary direct and indirect Tauc extrapolated energy gaps E_g^d and E_g^{i1} (Fig. 6A, green circles) span from 2.88–2.47 eV and 1.78–1.53 eV, respectively, for $x = 0$–14.4% compositions, red-shifting consistently with

increasing Ge. Linear extrapolation (to the normalized x-intercept) of the sub-gap absorption tail at energies below E_g^{i1} revealed an additional indirect absorption contribution E_g^{i2} (Fig. 6A, blue circles) between 1.16–1.10 eV for $x \leq 11.6\%$ and at 1.00 eV for $Si_{0.856}Ge_{0.144}$ NCs. The close proximity of these supplementary energy gaps to both the bulk Si and $Si_{1-x}Ge_x$ interpolated bandgaps (Fig. 6A, black dashed line) points toward the possible presence of residual larger, bulk-like particles within those samples and their likely relationship to E_g^{i2} absorption (ESI, Table S1†). The trend disparity of the $Si_{0.884}Ge_{0.116}$ composition is consistently observed for all energy gaps shown in Fig. 6A and Table 1 due to its smaller average diameter (5.9 ± 0.7 nm).

PL (Fig. 5 and ESI, Fig. S13 and S14†) was observed from all $Si_{1-x}Ge_x$ NCs ($x = 0$–14.4%) when excited at 405 nm, with peak energies ranging from 1.27–1.40 eV and an average full width at half maximum (FWHM) of 320 ± 50 meV (Fig. 5 and Table 1). Compared with distinct red-shifts noted in absorption with increasing Ge composition, little-to-no significant commensurate shifting in PL peak positions was observed for
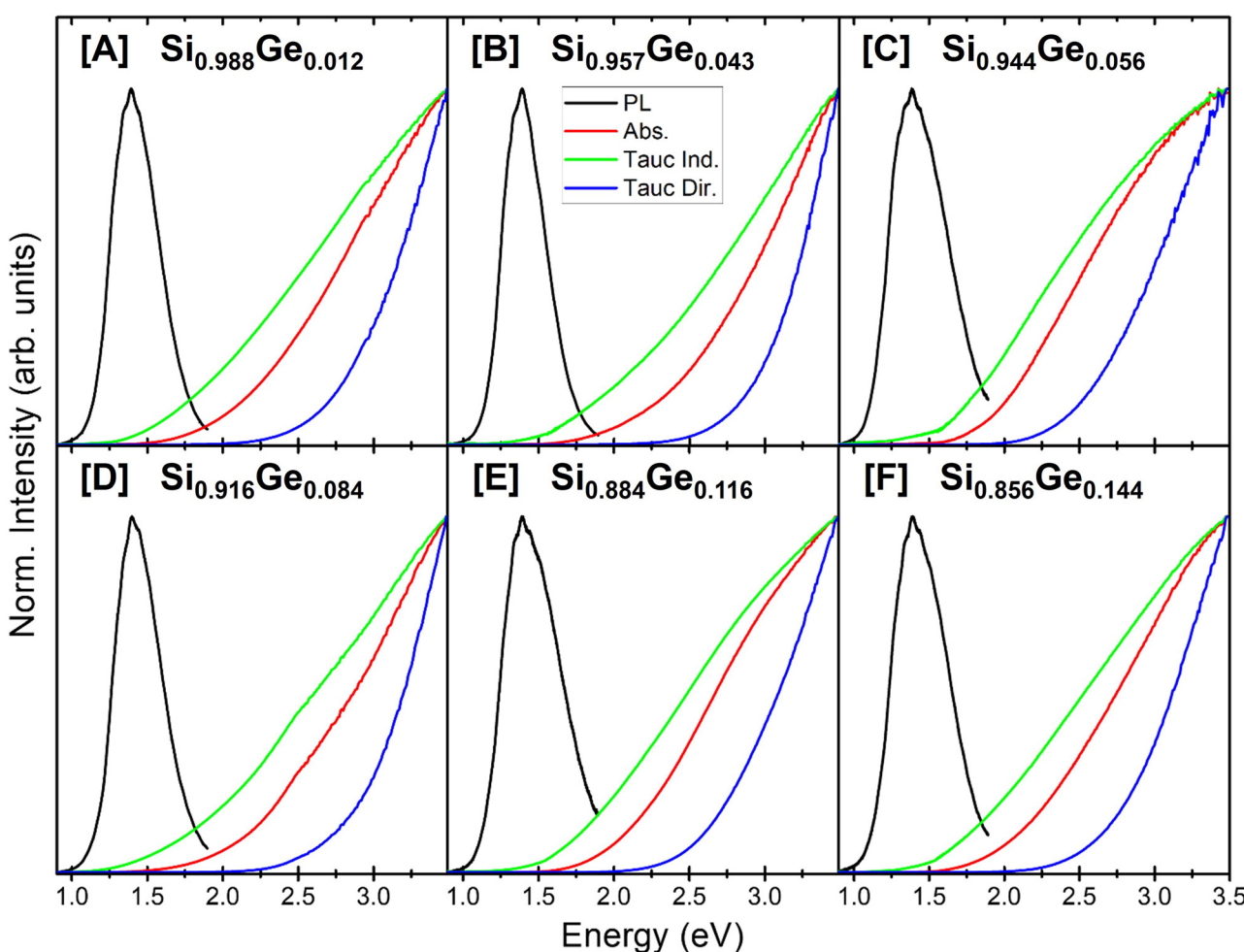
Fig. 5 Solid-state PL (black), Kubelka–Munk converted absorption (red), direct (blue) and indirect (green) Tauc spectra of [A] $Si_{0.988}Ge_{0.012}$, [B] $Si_{0.957}Ge_{0.043}$, [C] $Si_{0.944}Ge_{0.056}$, [D] $Si_{0.916}Ge_{0.084}$, [E] $Si_{0.884}Ge_{0.116}$, and [F] $Si_{0.856}Ge_{0.144}$ alloy NCs.

putational gaps predicted for variable $Si_{1-x}Ge_x$ compositions fall within the uncertainty range of PL energy gaps, indicating excellent agreement with each other. However, both the PL and computational energy gaps are smaller than those obtained from absorption onsets, with deviations of ~0.18 and ~0.21 eV, respectively. Notably, the absorption onset is smaller than the computational gap predicted for Ge NCs but larger than the computational gaps predicted for Si and $Si_{1-x}Ge_x$ NCs with x not equal to 1.0, a tendency consistent with the previous study.[33] Overall, a systematic decrease in the energy gaps was noted with increasing diameter and Ge content in the alloy NCs. A detailed comparison of the DFT-computed energy gaps and absorption/PL experimental data is shown in Table 1.

Conclusions

We have successfully developed a solid-state route for the synthesis of $Si_{1-x}Ge_x$ alloy NCs with variable compositions (x = 0–14.4%) *via* a relatively low temperature (600 °C) thermal disproportionation of a polymer-HSQ/GeI_2 composite precursor. The diameters of NCs were maintained within a narrow size range (5.9 ± 0.7–7.8 ± 1.1 nm) to correlate the physical properties to homogeneous alloying and alloy composition. HAADF images and STEM-EDS elemental maps confirm the homogeneous admixing of Si and Ge for alloys produced at 600 °C for 1 h whereas local segregation of Ge was observed at elevated temperatures (>800 °C) and longer growth times. PXRD and SAED patterns indicate a high crystallinity and phase purity of alloy NCs consistent with a diamond-cubic structure. Both the DFT computed and experimentally measured lattice parameters demonstrate a systematic expansion of Si structure upon Ge incorporation, consistent with the Vegard's law. Raman spectra indicate homogeneous alloying of isovalent elements realized by a red-shift of the Si–Si peak and the emergence of a Si–Ge/Ge–Ge peak with increasing Ge. XPS spectra revealed high-intensity Si^0/Ge^0 and Si–C/Ge–C peaks consistent with efficient hydrosilylation and hydrogermylation with dodecyl ligands. The energy gaps obtained from absorption onsets and Tauc direct and indirect analyses indicate composition-dependent red-shifts with increasing Ge and minor variations in PL peak energies. Any significant trends in PL peak maxima are potentially masked by size-dispersity and/or compositional variance. The theoretical energy gaps calculated for 7.2 nm $Si_{1-x}Ge_x$ alloys with variable compositions (x = 0–35%) are consistent with the experimental gaps obtained from PL studies. Moreover, both theoretical and experimental PL data indicate smaller gaps compared with the experimental absorption onsets, likely due to large Stokes shifts seen in Si-based nanostructures. This facile, low-temperature solid-state synthesis allows for the low-cost fabrication of discrete, quantum-confined $Si_{1-x}Ge_x$ alloys and thin films, which is more attractive than the previously used vapor deposition, MBE, and plasma-based methods, making it promising for a wider range of optical and electronic technologies. Specific studies to test these premises are currently underway.

Author contributions

G.S., R.M.F., and I.A. synthesized the NCs, examined their physical properties, and probed their solid-state absorbance. D.P. and U.O. measured PL from the NCs and analyzed optical properties and transitions. L.G. recorded the TEM images and Raman spectra. C.V. and K.U.L. probed theoretical energy gaps and lattice parameters. The manuscript was written/revised through contributions of all authors. All authors have given approval to the final version of the manuscript.

Data availability

The data supporting this article have been included as part of the ESI† as listed below. Additional raw data required to reproduce these findings can be made available upon request to the author.

Experimental parameters used in the synthesis of alloy NCs with variable compositions; low-energy Tauc indirect gaps, lattice parameters, and d-spacings of $Si_{1x}Ge_x$ alloy NCs; high-resolution TEM images, size histograms, SAED and zoomed-in PXRD patterns, SEM-EDS spectra, and Raman and solid state absorption spectra of Si and $Si_{1-x}Ge_x$ alloy NCs; STEM-HAADF elemental map overlays of $Si_{1-x}Ge_x$ NCs produced at different temperatures/times, PXRD patterns of $Si_{0.920}Ge_{0.080}$ (nominal composition) alloy NCs embedded in silica matrix and liberated after etching and hydrosilylation/hydrogermylation; XPS survey scans of colloidally stable Si and $Si_{0.856}Ge_{0.144}$ alloy NCs along with colloidally unstable $Si_{0.505}Ge_{0.495}$ alloy NCs; and Si 2p and Ge 3d XPS spectra of colloidally unstable $Si_{0.505}Ge_{0.495}$ alloy NCs, and solid-state PL and absorption spectra of Si NCs.

Conflicts of interest

The authors declare no competing financial interests.

Acknowledgements

References

1 A. S. Mahmood, K. Venkatakrishnan and B. Tan, *Sol. Energy Mater. Sol. Cells*, 2013, **115**, 58–63.
2 R. W. Crisp, N. Kirkwood, G. Grimaldi, S. Kinge, L. D. A. Siebbeles and A. J. Houtepen, *ACS Appl. Energy Mater.*, 2018, **1**, 6569–6576.
3 P. V. Kamat, *J. Phys. Chem. C*, 2008, **112**, 18737–18753.

4 H. Tran, T. Pham, J. Margetis, Y. Zhou, W. Dou, P. C. Grant, J. M. Grant, S. Al-Kabi, G. Sun, R. A. Soref, J. Tolle, Y.-H. Zhang, W. Du, B. Li, M. Mortazavi and S.-Q. Yu, *ACS Photonics*, 2019, **6**, 2807–2815.

5 X. Ji, H. Wang, B. Song, B. Chu and Y. He, *Front. Chem.*, 2018, **6**, 38.

6 J. Fan and P. K. Chu, *Small*, 2010, **6**, 2080–2098.

7 M. Sharma and S. K. Tripathi, *Appl. Phys. A*, 2013, **113**, 491–499.

8 S. Tallur and S. A. Bhave, *Nano Lett.*, 2013, **13**, 2760–2765.

9 D. S. Shen, J. P. Conde, V. Chu, S. Aljishi, J. Z. Liu and S. Wagner, *IEEE Electron Device Lett.*, 1992, **13**, 5–7.

10 R. J. A. Esteves, M. Q. Ho and I. U. Arachchige, *Chem. Mater.*, 2015, **27**, 1559–1568.

11 D. Z. Spera and I. U. Arachchige, *J. Phys. Chem. C*, 2022, **126**, 9862–9874.

12 R. C. Barbieri, K. Ding, Ü. Özgür and I. U. Arachchige, *Chem. Mater.*, 2021, **33**, 6897–6908.

13 G. C. Spence, R. C. Barbieri, D. Pate, L. S. Graves, Ü. Özgür and I. U. Arachchige, *J. Phys. Chem. C*, 2023, **127**, 11579–11590.

14 P. Reiss, M. Carrière, C. Lincheneau, L. Vaure and S. Tamang, *Chem. Rev.*, 2016, **116**, 10731–10819.

15 M. Lozac'h, V. Švrček, S. Askari, D. Mariotti, N. Ohashi, T. Koganezawa, T. Miyadera and K. Matsubara, *Mater. Today Energy*, 2018, **7**, 87–97.

16 L. T. Canham, *Appl. Phys. Lett.*, 1990, **57**, 1046–1048.

17 C. Delerue, G. Allan and M. Lannoo, *Phys. Rev. B: Condens. Matter Mater. Phys.*, 1993, **48**, 11024–11036.

18 C. M. Hessel, D. Reid, M. G. Panthani, M. R. Rasch, B. W. Goodfellow, J. Wei, H. Fujii, V. Akhavan and B. A. Korgel, *Chem. Mater.*, 2012, **24**, 393–401.

19 R. J. Clark, M. Aghajamali, C. M. Gonzalez, L. Hadidi, M. A. Islam, M. Javadi, M. H. Mobarok, T. K. Purkait, C. J. T. Robidillo, R. Sinelnikov, A. N. Thiessen, J. Washington, H. Yu and J. G. C. Veinot, *Chem. Mater.*, 2017, **29**, 80–89.

20 S. Terada, Y. Xin and K. Saitow, *Chem. Mater.*, 2020, **32**, 8382–8392.

21 J. Zhou, J. Huang, H. Chen, A. Samanta, J. Linnros, Z. Yang and I. Sychugov, *J. Phys. Chem. Lett.*, 2021, **12**, 8909–8916.

22 Y. Yu, G. Fan, A. Fermi, R. Mazzaro, V. Morandi, P. Ceroni, D.-M. Smilgies and B. A. Korgel, *J. Phys. Chem. C*, 2017, **121**, 23240–23248.

23 T. A. Pringle, K. I. Hunter, A. Brumberg, K. J. Anderson, J. A. Fagan, S. A. Thomas, R. J. Petersen, M. Sefannaser, Y. Han, S. L. Brown, D. S. Kilin, R. D. Schaller, U. R. Kortshagen, P. R. Boudjouk and E. K. Hobbie, *ACS Nano*, 2020, **14**, 3858–3867.

24 D. M. Lyons, K. M. Ryan, M. A. Morris and J. D. Holmes, *Nano Lett.*, 2002, **2**, 811–816.

25 J. D. Holmes, K. P. Johnston, R. C. Doty and B. A. Korgel, *Science*, 2000, **287**, 1471–1473.

26 A. L. Holmes, J. Hütges, A. Reckmann, E. Muthuswamy, K. Meerholz and S. M. Kauzlarich, *J. Phys. Chem. C*, 2015, **119**, 5671–5678.

27 J. D. Holmes, K. J. Ziegler, R. C. Doty, L. E. Pell, K. P. Johnston and B. A. Korgel, *J. Am. Chem. Soc.*, 2001, **123**, 3743–3748.

28 R. J. Alan Esteves, S. Hafiz, D. O. Demchenko, Ü. Özgür and I. U. Arachchige, *Chem. Commun.*, 2016, **52**, 11665–11668.

29 K. Ramasamy, P. G. Kotula, A. F. Fidler, M. T. Brumbach, J. M. Pietryga and S. A. Ivanov, *Chem. Mater.*, 2015, **27**, 4640–4649.

30 V. Tallapally, T. A. Nakagawara, D. O. Demchenko, Ü. Özgür and I. U. Arachchige, *Nanoscale*, 2018, **10**, 20296–20305.

31 W. Du and S.-Q. Yu, in *Mid-infrared Optoelectronics*, ed. E. Tournié and L. Cerutti, Woodhead Publishing, 2020, pp. 493–538.

32 D. Spera, D. Pate, G. C. Spence, C. Villot, C. J. Onukwughara, D. White, K. U. Lao, Ü. Özgür and I. U. Arachchige, *Chem. Mater.*, 2023, **35**, 9007–9018.

33 D. O. Demchenko, V. Tallapally, R. J. A. Esteves, S. Hafiz, T. A. Nakagawara, I. U. Arachchige and Ü. Özgür, *J. Phys. Chem. C*, 2017, **121**, 18299–18306.

34 V. Švrček, D. Mariotti, R. A. Blackley, W. Z. Zhou, T. Nagai, K. Matsubara and M. Kondo, *Nanoscale*, 2013, **5**, 6725–6730.

35 A. M. Chockla, K. C. Klavetter, C. B. Mullins and B. A. Korgel, *Chem. Mater.*, 2012, **24**, 3738–3745.

36 X. Lu, C. M. Hessel, Y. Yu, T. D. Bogart and B. A. Korgel, *Nano Lett.*, 2013, **13**, 3101–3105.

37 J. P. Dismukes, L. Ekstrom and R. J. Paff, *J. Phys. Chem.*, 1964, **68**, 3021–3027.

38 R. Braunstein, A. R. Moore and F. Herman, *Phys. Rev.*, 1958, **109**, 695–710.

39 M. Virgilio and G. Grosso, *J. Phys.: Condens. Matter*, 2006, **18**, 1021–1031.

40 S. Takeoka, K. Toshikiyo, M. Fujii, S. Hayashi and K. Yamamoto, *Phys. Rev. B: Condens. Matter Mater. Phys.*, 2000, **61**, 15988–15992.

41 A. Md. Asaduzzaman and M. Springborg, *Phys. Rev. B: Condens. Matter Mater. Phys.*, 2006, **74**, 165406.

42 H. ur Rehman, M. Springborg and Y. Dong, *J. Phys. Chem. A*, 2011, **115**, 2005–2015.

43 B. G. Walker, S. C. Hendy and R. D. Tilley, *Eur. Phys. J. B*, 2009, **72**, 193–201.

44 C. Schwinge, K. Kühnel, J. Emara, L. Roy, K. Biedermann, W. Weinreich, S. Kolodinski, M. Wiatr, G. Gerlach and M. Wagner-Reetz, *Appl. Phys. Lett.*, 2022, **120**, 031903.

45 R. Cheaito, J. C. Duda, T. E. Beechem, K. Hattar, J. F. Ihlefeld, D. L. Medlin, M. A. Rodriguez, M. J. Campion, E. S. Piekos and P. E. Hopkins, *Phys. Rev. Lett.*, 2012, **109**, 195901.

46 E. Kasper, J. Werner, M. Oehme, S. Escoubas, N. Burle and J. Schulze, *Thin Solid Films*, 2012, **520**, 3195–3200.

47 L. Wei, H. Zhang, L. Shi and Z. Yang, *Nanoscale*, 2024, **16**, 6516–6521.

48 Y. S. Tang, S. Cai, G. Jin, J. Duan, K. L. Wang, H. M. Soyez and B. S. Dunn, *Appl. Phys. Lett.*, 1997, **71**, 2448–2450.

49 E. J. Henderson and J. G. C. Veinot, *Chem. Mater.*, 2007, **19**, 1886–1888.

50 S. D. Barry, Z. Yang, J. A. Kelly, E. J. Henderson and J. G. C. Veinot, *Chem. Mater.*, 2011, **23**, 5096–5103.

51 M. Alfredo and C. Lieber, *Science*, 1998, **279**, 208–211.

52 R. J. Petersen, S. A. Thomas, K. J. Anderson, T. A. Pringle, S. May and E. K. Hobbie, *J. Phys. Chem. C*, 2022, **126**, 12935–12943.

53 J. Niu, J. Sha and D. Yang, *Phys. E*, 2004, **23**, 131–134.

54 C. M. Hessel, E. J. Henderson and J. G. C. Veinot, *Chem. Mater.*, 2006, **18**, 6139–6146.

55 C. M. Hessel, J. Wei, D. Reid, H. Fujii, M. C. Downer and B. A. Korgel, *J. Phys. Chem. Lett.*, 2012, **3**, 1089–1093.

56 C. Cibaka-Ndaya, K. O'Connor, E. O. Idowu, M. A. Parker, E. Lebraud, S. Lacomme, D. Montero, P. S. Camacho, J. G.-C. Veinot, I.-L. Roiban and G. L. Drisko, *Chem. Mater.*, 2023, **35**, 8551–8560.

57 D. S. Pate, G. C. Spence, L. S. Graves, I. U. Arachchige and Ü. Özgür, *J. Phys. Chem. C*, 2024, **128**, 10483–10491.

58 D. T. Restrepo, K. E. Lynch, K. Giesler, S. M. Kuebler and R. G. Blair, *Mater. Res. Bull.*, 2012, **47**, 3484–3488.

59 B. Kowalczyk, I. Lagzi and B. A. Grzybowski, *Curr. Opin. Colloid Interface Sci.*, 2011, **16**, 135–148.

60 S. Gravelsins and A.-A. Dhirani, *RSC Adv.*, 2017, **7**, 55830–55834.

61 H. Borchert, E. V. Shevchenko, A. Robert, I. Mekis, A. Kornowski, G. Grübel and H. Weller, *Langmuir*, 2005, **21**, 1931–1936.

62 A. H. Larsen, J. J. Mortensen, J. Blomqvist, I. E. Castelli, R. Christensen, M. Dułak, J. Friis, M. N. Groves, B. Hammer, C. Hargus, E. D. Hermes, P. C. Jennings, P. B. Jensen, J. Kermode, J. R. Kitchin, E. L. Kolsbjerg, J. Kubal, K. Kaasbjerg, S. Lysgaard, J. B. Maronsson, T. Maxson, T. Olsen, L. Pastewka, A. Peterson, C. Rostgaard, J. Schiøtz, O. Schütt, M. Strange, K. S. Thygesen, T. Vegge, L. Vilhelmsen, M. Walter, Z. Zeng and K. W. Jacobsen, *J. Phys.: Condens. Matter*, 2017, **29**, 273002.

63 J. P. Wilcoxon, G. A. Samara and P. N. Provencio, *Phys. Rev. B: Condens. Matter Mater. Phys.*, 1999, **60**, 2704–2714.

64 C. S. Garoufalis, A. D. Zdetsis and S. Grimme, *Phys. Rev. Lett.*, 2001, **87**, 276402.

65 C. S. Garoufalis and A. D. Zdetsis, *Phys. Chem. Chem. Phys.*, 2006, **8**, 808–813.

66 S. Krishnamurthy, A. Sher and A. Chen, *Appl. Phys. Lett.*, 1985, **47**, 160–162.

67 J. Weber and M. I. Alonso, *Phys. Rev. B: Condens. Matter Mater. Phys.*, 1989, **40**, 5683–5693.

68 B. Bonham and G. Guisbiers, *Nanotechnology*, 2017, **28**, 245702.

69 O. Yasar-Inceoglu and L. Mangolini, *Mater. Lett.*, 2013, **101**, 76–79.

70 F. Erogbogbo, T. Liu, N. Ramadurai, P. Tuccarione, L. Lai, M. T. Swihart and P. N. Prasad, *ACS Nano*, 2011, **5**, 7950–7959.

71 C.-W. Lin, S.-Y. Lin, S.-C. Lee and C.-T. Chia, *J. Appl. Phys.*, 2002, **91**, 2322–2325.

72 M. Kobayashi, G. Thareja, M. Ishibashi, Y. Sun, P. Griffin, J. McVittie, P. Pianetta, K. Saraswat and Y. Nishi, *J. Appl. Phys.*, 2009, **106**, 104117.

73 X. Zhu, G. H. ten Brink, S. de Graaf, B. J. Kooi and G. Palasantzas, *Chem. Mater.*, 2020, **32**, 1627–1635.

74 K. Dohnalová, T. Gregorkiewicz and K. Kůsová, *J. Phys.: Condens. Matter*, 2014, **26**, 173201.

75 D. C. Cronemeyer, *J. Appl. Phys.*, 1958, **29**, 1730–1735.

76 S. J. Rathi, B. N. Jariwala, J. D. Beach, P. Stradins, P. C. Taylor, X. Weng, Y. Ke, J. M. Redwing, S. Agarwal and R. T. Collins, *J. Phys. Chem. C*, 2011, **115**, 3833–3839.

77 K. R. Williams and R. S. Muller, *J. Microelectromech. Syst.*, 1996, **5**, 256–269.

78 K. W. Kolasinski, *Surf. Sci.*, 2009, **603**, 1904–1911.

79 V. Caubet, C. Beylier, S. Borel and O. Renault, *J. Vac. Sci. Technol., B:Microelectron. Nanometer Struct.–Process., Meas., Phenom.*, 2006, **24**, 2748–2754.

80 A. A. Shklyaev and K. E. Ponomarev, *J. Cryst. Growth*, 2015, **413**, 94–99.

81 E. C. Frey, N. R. Parikh, M. L. Swanson, M. Z. Numan and W. K. Chu, *MRS Online Proc. Libr.*, 1987, **105**, 277–282.

82 D. A. Grützmacher, T. O. Sedgwick, A. Powell, M. Tejwani, S. S. Iyer, J. Cotte and F. Cardone, *Appl. Phys. Lett.*, 1993, **63**, 2531–2533.

83 C. M. Hessel, E. J. Henderson and J. G. C. Veinot, *J. Phys. Chem. C*, 2007, **111**, 6956–6961.

84 A. C. Meng, C. S. Fenrich, M. R. Braun, J. P. McVittie, A. F. Marshall, J. S. Harris and P. C. McIntyre, *Nano Lett.*, 2016, **16**, 7521–7529.

85 A. Garcia-Gil, S. Biswas, D. McNulty, A. Roy, K. M. Ryan, V. Nicolosi and J. D. Holmes, *Adv. Mater. Interfaces*, 2022, **9**, 2201170.

86 I. T. Cheong, L. Y. Szepesvari, C. Ni, C. Butler, K. M. O'Connor, R. Hooper, A. Meldrum and J. G. C. Veinot, *Nanoscale*, 2024, **16**, 592–603.

87 K. Hummer, J. Harl and G. Kresse, *Phys. Rev. B: Condens. Matter Mater. Phys.*, 2009, **80**, 115205.

88 J.-H. Pöhls, M. Heyberger and A. Mar, *J. Solid State Chem.*, 2020, **290**, 121557.

89 I. M. Joni, L. Nulhakim, M. Vanitha and C. Panatarani, *J. Phys.: Conf. Ser.*, 2018, **1080**, 012006.

90 B. J. Stacy, S. V. Shah, A. De Gorostiza, L. Ngo and B. A. Korgel, *ACS Mater. Lett.*, 2024, **6**, 73–80.

91 K. Tabatabaei, A. L. Holmes, K. A. Newton, E. Muthuswamy, R. Sfadia, S. A. Carter and S. M. Kauzlarich, *Chem. Mater.*, 2019, **31**, 7510–7521.

92 M. R. Arghavani, R. Braunstein, G. Chalmers, D. Shirun and P. Yang, *Solid State Commun.*, 1989, **71**, 599–601.

93 C. M. Hessel, M. R. Rasch, J. L. Hueso, B. W. Goodfellow, V. A. Akhavan, P. Puvanakrishnan, J. W. Tunnel and B. A. Korgel, *Small*, 2010, **6**, 2026–2034.

94 E. J. Henderson and J. G. C. Veinot, *J. Am. Chem. Soc.*, 2009, **131**, 809–815.

95 A. Avila, I. Montero, L. Galán, J. M. Ripalda and R. Levy, *J. Appl. Phys.*, 2001, **89**, 212–216.

96 V. Kalimuthu, P. Kumar, M. Kumar and S. Rath, *Appl. Phys. A*, 2018, **124**, 712.

97 A. S. Almuslem, A. N. Hanna, T. Yapici, N. Wehbe, E. M. Diallo, A. T. Kutbee, R. R. Bahabry and M. M. Hussain, *Appl. Phys. Lett.*, 2017, **110**, 074103.

98 M. Grodzicki, A. K. Tołłoczko, D. Majchrzak, D. Hommel and R. Kudrawiec, *Crystals*, 2022, **12**, 1492.

99 H. Yu, T. Helbich, L. M. Scherf, J. Chen, K. Cui, T. F. Fässler, B. Rieger and J. G. C. Veinot, *Chem. Mater.*, 2018, **30**, 2274–2280.

100 A. Tsuge, Y. Uwamino, T. Ishizuka and K. Suzuki, *Appl. Spectrosc.*, 1991, **45**, 1377–1380.

101 P. Y. Yu and M. Cardona, *Fundamentals of Semiconductors: Physics and Materials Properties*, Springer, Berlin, 2010.

102 D. Carolan, *Prog. Mater. Sci.*, 2017, **90**, 128–158.

103 B. R. Taylor, S. M. Kauzlarich, G. R. Delgado and H. W. H. Lee, *Chem. Mater.*, 1999, **11**, 2493–2500.

104 D. S. Pate, G. C. Spence, L. S. Graves, I. U. Arachchige and Ü. Özgür, *J. Phys. Chem. C*, 2024, **128**, 10483–10491.

105 I. Robel, R. Gresback, U. Kortshagen, R. D. Schaller and V. I. Klimov, *Phys. Rev. Lett.*, 2009, **102**, 177404.

106 D. A. Ruddy, J. C. Johnson, E. R. Smith and N. R. Neale, *ACS Nano*, 2010, **4**, 7459–7466.

107 K.-Y. Cheng, R. Anthony, U. R. Kortshagen and R. J. Holmes, *Nano Lett.*, 2011, **11**, 1952–1956.

108 O. Millo, I. Balberg, D. Azulay, T. K. Purkait, A. K. Swarnakar, E. Rivard and J. G. C. Veinot, *J. Phys. Chem. Lett.*, 2015, **6**, 3396–3402.

109 S. A. Sami and N. A. Abdulkarim, *Mater. Res. Bull.*, 2021, **142**, 111428.